

This article appeared in a journal published by Elsevier. The attached copy is furnished to the author for internal non-commercial research and education use, including for instruction at the authors institution and sharing with colleagues.

Other uses, including reproduction and distribution, or selling or licensing copies, or posting to personal, institutional or third party websites are prohibited.

In most cases authors are permitted to post their version of the article (e.g. in Word or Tex form) to their personal website or institutional repository. Authors requiring further information regarding Elsevier's archiving and manuscript policies are encouraged to visit:

<http://www.elsevier.com/copyright>



Contents lists available at ScienceDirect

Icarus

journal homepage: www.elsevier.com/locate/icarus



Machine cataloging of impact craters on Mars

Tomasz F. Stepinski^{a,*}, Michael P. Mendenhall^b, Brian D. Bue^c

^a Lunar and Planetary Institute, 3600 Bay Area Blvd., Houston, TX 77058, USA

^b Department of Physics 103-33, Caltech, Pasadena, CA 91125, USA

^c Jet Propulsion Laboratory, 4800 Oak Grove Drive, Pasadena, CA 91109, USA

ARTICLE INFO

Article history:

Received 21 March 2007

Revised 31 March 2009

Accepted 2 April 2009

Available online 22 May 2009

Keywords:

Cratering

Mars, Surface

ABSTRACT

This study presents an automated system for cataloging impact craters using the MOLA 128 pixels/degree digital elevation model of Mars. Craters are detected by a two-step algorithm that first identifies round and symmetric topographic depressions as crater candidates and then selects craters using a machine-learning technique. The system is robust with respect to surface types; craters are identified with similar accuracy from all different types of martian surfaces without adjusting input parameters. By using a large training set in its final selection step, the system produces virtually no false detections. Finally, the system provides a seamless integration of crater detection with its characterization. Of particular interest is the ability of our algorithm to calculate crater depths. The system is described and its application is demonstrated on eight large sites representing all major types of martian surfaces. An evaluation of its performance and prospects for its utilization for global surveys are given by means of detailed comparison of obtained results to the manually-derived Catalog of Large Martian Impact Craters. We use the results from the test sites to construct local depth–diameter relationships based on a large number of craters. In general, obtained relationships are in agreement with what was inferred on the basis of manual measurements. However, we have found that, in Terra Cimmeria, the depth/diameter ratio has an abrupt decrease at $\sim 38^\circ\text{S}$ regardless of crater size. If shallowing of craters is attributed to presence of sub-surface ice, a sudden change in its spatial distribution is suggested by our findings.

© 2009 Elsevier Inc. All rights reserved.

1. Introduction

Martian craters display great variety and complexity of morphologies because of the wide range of ages on the surfaces on which they are located and multiplicity of degradational processes to which they are subjected. Detailed analysis of craters' morphology and their spatial statistics is an important source of information about geologic processes and properties of martian surfaces. Regional differences in crater size distributions form the basis for geological stratigraphy of Mars (Crater Analysis Technique Working Group, 1979; Wise and Minkowski, 1980; Tanaka, 1986; Hartmann and Neukum, 2001). Craters are natural probes of target surface properties; spatial variations in crater morphologies indicate variations in geologic material (Cintala et al., 1976), including the presence of sub-surface volatiles (Cintala and Mouginis-Mark, 1980; Kieffer and Simonds, 1980; Kuzmin et al., 1988; Costard, 1989; Mouginis-Mark and Hayashi, 1993; Barlow and Perez, 2003; Barlow, 2005; Reiss et al., 2006). In addition, the nature, timing, and location of past surficial processes are inferred from observed crater morphologies and their spatial distributions (Soderblom et al., 1974; Craddock et al., 1997; Boyce et al.,

2005). For all of these reasons, impact craters are among the most studied features on Mars, and a number of catalogs listing crater positions and their morphological attributes have been compiled (Barlow, 1988; Costard, 1989; Kuzmin et al., 1988; Roddy et al., 1998; Rodionova et al., 2000; Salamuniccar and Loncaric, 2008) to facilitate the crater-related research. These datasets, some global while others regional in extent, are all based on visual inspection of images. The image-based catalogs provide numerical parameters pertaining to planar geometry of craters and categorical parameters pertaining to their observed morphologies, but they lack any information about crater depths and other topographical parameters. The most widely used image-based dataset is *The Catalog of Large Martian Impact Craters* (Barlow, 1988) (hereafter referred to as the Barlow catalog). It lists locations and eight parameters for 42,283 craters distributed over all of Mars. Another global dataset is the *Morphological Catalogue of the Craters of Mars* (Rodionova et al., 2000) that lists locations and 15 parameters for 19,308 craters. The positions of craters in these two catalogs are not aligned with actual craters as registered in the more modern imagery and topographic data conforming to the Mars Digital Image Model (MDIM) 2.1 standard. Recently, Salamuniccar and Loncaric (2008) have corrected the subsets of the two aforementioned catalogs and compiled a catalog of 57,633 craters that conforms to the MDIM 2.1 standard. It is worth noting that a revision

* Corresponding author. Fax: +1 281 486 2162.

E-mail address: tom@lpi.usra.edu (T.F. Stepinski).

(Barlow, 2006) of the *The Catalog of Large Martian Impact Craters* is currently in progress; the revised catalog will list location of craters that conforms to the MDIM 2.1 standard and provide updated and more extensive description of the craters.

The lack of information about crater depths, and, to a lesser degree, non-adherence to the MDIM 2.1 standard, limits the utility of presently available global crater catalogs. Crater depths must be calculated for individual projects as needed, resulting in a limited, and highly segmented dataset of craters for which depths have been acquired by a variety of methods with different standards of accuracy. The photoclinometric technique was used by Pike and Davis (1984), Mouginis-Mark and Hayashi (1993), and Craddock et al. (1997). Garvin and Frawley (1998), Garvin et al. (2000), and Forsberg-Taylor et al. (2004) used individual altimetric profiles obtained by the Mars Orbiter Laser Altimeter (MOLA). Finally, Mouginis-Mark et al. (2004) and Stewart and Valiant (2006) calculated crater depths from a MOLA-based digital elevation model (DEM). In order to take a full advantage of information contained in martian crater record, a new global catalog of martian craters, listing topographic parameters (such as crater depths) needs to be compiled. Automating the process of crater identification and characterization would significantly expedite such an update. A robust crater identification algorithm provides consistency unattainable by human catalogers, and it is the only practical means of extending the crater dataset to smaller craters.

In this paper, we present a robust automated crater detection and characterization system (hereafter referred to as the AutoCrat system). The aim of the AutoCrat system is twofold. First, to provide a robust means for machine identification of craters that could be applied for global cataloging with accuracy on par with or exceeding the accuracy of existing, manually assembled catalogs. Second, to automatically characterize the identified craters, including calculating their depths. In order to achieve these goals, the AutoCrat is the first topography-based crater detection algorithm (CDA). Existing research on CDAs focuses almost exclusively on image-based algorithms (Barata et al., 2004; Burl et al., 2001; Cheng et al., 2003; Honda et al., 2002; Kim et al., 2005; Leroy et al., 2001; Plesko et al., 2004; Vinogradova et al., 2002; Wetzler et al., 2005). Image-based CDAs are quite involved because of inherent limitations of imagery data; the “visibility” of an impact crater depends on the quality of an image, which, in turn, depends on illumination, surface properties, and atmospheric state. Although some of these CDAs have shown good accuracy when applied to selected test sites, none was shown to be robust enough to accommodate all different kinds of martian surfaces making them inadequate for a global cataloging project.

We have proposed (Bue and Stepinski, 2007) basing a CDA on topographic rather than imagery data on the premise that topographic data is better suited for machine processing since craters have more direct expressions in topography than they do in images. In other words, identifying craters as topographic depressions should be more robust than identifying them as circular shapes in an image. However, identifying individual depressions proved to be a challenge, so although a CDA developed by Bue and Stepinski (2007) uses depressions to simplify the calculations, the actual identification of craters is performed by looking for circular features in an image depicting topographic curvature. The reliance on recognition of planar circular patterns limits robustness of this CDA. We have since developed a method to identify single topographic depressions irrespective of their scale and degree to which they are nested in each other, thus the AutoCrat identifies craters directly as topographic depressions. Using a manually defined decision function to separate craters from other crater-like features also decreases the robustness of a CDA. Such a function consists of rules identified while manually examining a limited number of craters, and are

unlikely to apply to larger collection of craters. In the AutoCrat we use machine-learning techniques to derive the decision function as accurately as possible.

This paper focuses on describing (in Section 2) the methods used in the AutoCrat system, and means to cross-reference its results with the Barlow catalog. We have applied the AutoCrat to eight diverse sites totaling $1.45 \times 10^8 \text{ km}^2$ or 4.6% of the martian surface representing Noachian, Hesperian, as well as Amazonian surfaces. In an effort to assess the feasibility of the AutoCrat for global cataloging of craters we offer comprehensive analysis of the results (Section 3) including a detailed comparison to the Barlow catalog, and accuracy evaluation of calculated crater diameters and depths. We then proceed to calculate depth–diameter relationships for the eight regions in our study (Section 4), discuss their statistics, and compare them to similar relations calculated previously for other regions on Mars. Discussion and conclusions follows in Section 5.

2. Crater detection methodology

The AutoCrat system consists of two major modules: a rule-based, topographic depression-finding algorithm, and a machine-learning crater-selecting algorithm. This modular architecture separates the two major challenges facing all feature-finding algorithms, completeness (minimization of false negative detections) and accuracy (minimization of false positive detections). In our context, false negatives are craters not identified by the system, and false positives are non-crater features identified by the system as craters.

The rule-based module of the AutoCrat system is designed to address the completeness issue. The core concept behind this module is that all craters are topographic depressions. Thus, the role of this module is to identify all topographic depressions in a given site, including superposed depressions and irregular depressions. Only a subset of identified depressions consist of actual craters. The rule-based module also performs the preliminary separation of craters from non-crater depressions using manually defined rules. Defining a single set of rules that work equally well for all foreseeable martian surfaces is not feasible. Indeed, lack of robustness of previous, image-based automated CDAs can be attributed, in large part, to difficulties in designing a “one-size-fits-all” set of rules for accepting an object as a crater. In our rule-based module such rules are purposely lax, designed to reject only clearly non-crater depressions, and to accept as “craters” even marginally plausible depressions. The outcome of the rule-based module is a list of crater candidates containing, as its subset, true craters registering as topographic depressions.

The machine-learning module of the AutoCrat system is designed to address the accuracy issue by extracting true craters from the list of crater candidates as precisely as possible. It utilizes a supervised machine-learning technique to assign all crater candidates either a crater or a non-crater label. This technique relies on a training set of depressions, for which an expert has already assigned the labels, to construct a labeling function that is then applied to label all other crater candidates. The labeling function is a very extensive, computer-derived set of rules that reflects a connection between numerical attributes of crater candidates and their labels as assigned on the basis of expert reasoning. Given a representative and extensive training set, a machine-learning module can separate craters from non-craters with precision unattainable by any manually defined set of rules.

The AutoCrat uses the Mission Experiment Gridded Data Record (MEGDR) (Smith et al., 2003) with resolution of $1/128^\circ$ as the input data. The site of interest is extracted from the MEGDR in the form of a DEM—a raster of elevation values. We refer to such a raster as

“landscape” and denote it by $Z(\vec{x})$; the vector \vec{x} denotes pixel's location in Z .

2.1. Identifying topographic depressions

In principle, topographic depressions in a landscape could be identified by the “flooding” algorithm (O’Callaghan and Mark, 1984). The flooding algorithm identifies depressions in the landscape by raising elevation of pixels within them to the level of the lowest pour point. However, Bue and Stepinski (2007) have pointed out that flooding algorithm cannot be utilized as an accurate depression-finder in actual martian landscapes because superposed depressions, common in such landscapes, are identified as a single depression by the flooding algorithm.

In AutoCrat, the problem of nested depressions is addressed by first identifying only the smallest depressions, then proceeding to identification of successively larger depressions in subsequent steps. In order to separate depressions of different scales we introduce a function (hereafter referred to as the C-transform) that transforms the original landscape $Z(\vec{x})$ into an artificial landscape $C_\lambda(\vec{x})$ optimized for identification of depressions having a length scale λ . The core concept behind the C-transform is that it calculates a degree to which elevation gradients anchored to pixels in the λ -size neighborhood of the focal pixel \vec{x} are aligned to point toward that pixel. The C-transform is given by the following formula,

$$C_\lambda(\vec{x}) = \int \int_Z e^{-\frac{|\vec{x}-\vec{x}'|^2}{2\lambda^2}} \nabla Z(\vec{x}') \cdot \frac{\vec{x}' - \vec{x}}{|\vec{x}' - \vec{x}|} d\vec{x}' \quad (1)$$

Depressions of size $\sim \lambda$ form smooth, pronounced basins in the transformed landscape. However, features having scale smaller than λ are smoothed out, and features having scale bigger than λ are suppressed. We refer to the C_λ rasters as layers; topographic depressions in the landscape Z , having characteristic size λ_0 , are identified as the upward-concave regions in the co-registered C_{λ_0} layer. Concavity is determined by calculating the discrete second derivative along four lines (horizontal, vertical, and two diagonals) through each pixel in the layer; the pixels with positive second derivative in all four directions are considered to be upward-concave. The single-connected regions of upward-concave pixels mark individual topographic depressions of scale λ_0 . Spatial extents of such regions tend to be smaller than the extents of the entire topographic depressions they indicate because the outer reaches of depressions are often downward-concave in contrast to their upward-concave interiors. To assure the proper size of identified depressions we expand each region outward until it fills the entire extent of the depression. This expansion is achieved using a cellular-automata-like approach in which a region aggregates neighboring pixels subject to a threshold that stops the buildup when the expansion proceeds for too long over slopes that are too low.

This depression-finding procedure is repeated for N layers $C_{\lambda_1}, \dots, C_{\lambda_N}$. The smallest depressions are identified from the C_{λ_1} layer. The value of $\lambda_1 = 5$ pixels has been chosen in order for the smallest identified depressions to have diameters of about 10 pixels or 5 km. In practice, this choice results in finding depressions with diameters even smaller than 5 km. Each subsequent layer is characterized by $\lambda_{k+1} = 2\lambda_k$; the value of λ_N is limited by the smaller dimension of the raster Z .

The planar attributes of each identified depression, U , are determined from its geometrical properties. The location of the center of the depression \vec{c} is calculated from its centroid,

$$\vec{c} = \frac{\int \int_U \vec{x} d\vec{x}}{\int \int_U d\vec{x}} \quad (2)$$

The shape of a depression's edge is described by the polar function $r(\theta)$ with the origin located at \vec{c} . In order to describe this shape in terms of just a few numbers we calculate its Fourier expansion,

$$r(\theta) = r_0 \cdot \left(1 + \sum_{k=1}^{\infty} a_k \cos k\theta + b_k \sin k\theta \right) \quad (3)$$

where

$$\pi r_0^2 \equiv \int \int_U d\vec{x}; \quad a_k \equiv \frac{\int \int_U \cos k\theta d\vec{x}}{\int \int_U d\vec{x}}; \quad b_k \equiv \frac{\int \int_U \sin k\theta d\vec{x}}{\int \int_U d\vec{x}}$$

The coefficient r_0 estimates the radius of the depression, whereas the coefficients a_k , and b_k pertain to its shape. Note that $a_1 \approx 0$ and $b_1 \approx 0$ due to the choice of the origin at \vec{c} , so the leading shape coefficients are a_2 and b_2 .

In addition to calculating a depression's planar properties, we also calculate the planar properties of the field of elevation gradients within the depression. The average gradient $\vec{g}(\theta)$ is a function of a polar angle around the centroid \vec{c} . It is an average of elevation gradients at all pixels located along a θ -ray anchored at \vec{c} and terminating at the edge of the depression. We expand $\vec{g}(\theta)$ into a Fourier series,

$$\vec{g}(\theta) = \sum_{k=0}^{\infty} (a_k^g \cos k\theta + b_k^g \sin k\theta) \hat{x} + \sum_{k=0}^{\infty} (c_k^g \cos k\theta + d_k^g \sin k\theta) \hat{y} \quad (4)$$

Expansion coefficients describe the symmetry, or lack thereof, of gradient fields within the depression. For a round and symmetric depression (an ideal crater) a_1^g and d_1^g are the dominant coefficients, while $a_0^g \hat{x} + c_0^g \hat{y}$ gives the average background slope of the region where the depression is located. Larger magnitudes of other coefficients reflect a departure from symmetry and indicate that the depression may not be a crater.

Each identified depression is subject to verification using a set of seven hand-made rules utilizing values of shape and $\vec{g}(\theta)$ expansion coefficients. These rules are designed to flag depressions that are clearly non-crater features because they are too elongated, too lumpy, or their gradient fields are too asymmetric with respect to our settings. Depressions passing verification criteria are assigned unique identification labels and a number of attributes including its centroid, all expansion coefficients, as well as their depths. The lists of depressions identified in all layers are concatenated into a single list of crater candidates.

Fig. 1 illustrates the procedure described in this sub-section. The sample site is centered at the Tisia Valles region (46.13°E and 11.83°S). It is approximately 215 km west to east and 192 km south to north, so the AutoCrat has calculated six layers up to $\lambda_6 = 160$ pixels. No depression in layers $C_{\lambda \geq \lambda_4}$ has passed the verification test, so Fig. 1 shows only results from the first three layers. The first column shows the actual landscape, the second column shows the three optimized landscapes (layers), the third column shows the unexpanded depressions identified in each layer, and the fourth column shows expanded depressions that have passed the verification test. Note that the large, irregular, and heavily degraded crater located on the right edge of the sample site is identified as a depression in C_{λ_4} but does not pass the verification test with the default settings.

2.2. Selecting craters

No hand-made set of rules is robust enough to distinguish craters from non-crater depressions with high precision in all different kinds of martian surfaces. This is why we turn to machine-learning for the final selection of craters from the list of crater candidates. The machine-learning technique enables automatic

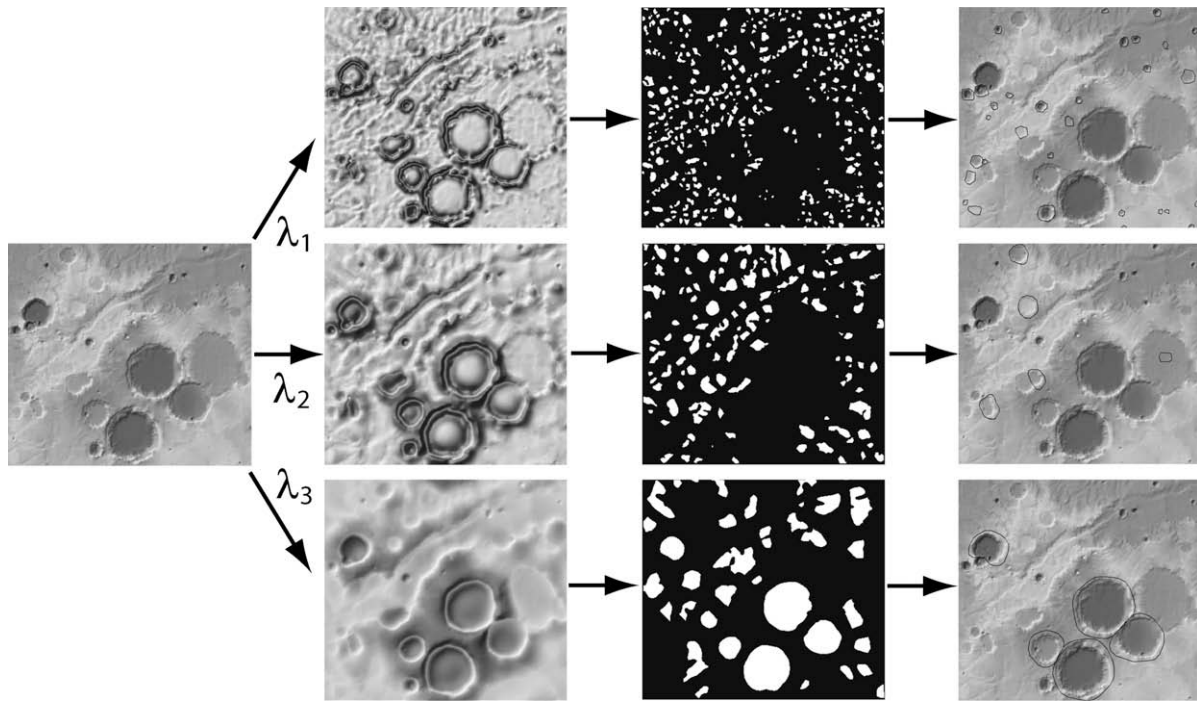


Fig. 1. Identification of crater candidates from topographic data. (Left) Topography of the Tisia Valles site on Mars. (Center left) Three optimized landscapes (layers) corresponding to λ_1 , λ_2 and λ_3 , respectively. (Center right) Unexpanded depressions identified in the first three layers. (Right) Expanded depressions that passed the verification test.

(or semi-automatic) pattern recognition in data (Witten and Frank, 2000). In our context data is the list of crater candidates and we are focusing on classification learning (also known as supervised learning)—a scheme that “learns” how to classify crater candidates into either a crater class or a non-crater class from a set of previously classified examples (called a training set). Each crater candidate has been assigned a list of numerical attributes (see the previous sub-section). We use these attributes to derive a shorter list of classification attributes $\{D, d, d/D, m_2, m_3, class\}$ for use by the machine-learning algorithm. Here D is candidate’s diameter, d is its depth, $m_2 = \sqrt{a_2^2 + b_2^2}$ describes elongation of candidate’s planar shape, and $m_3 = \sqrt{a_3^2 + b_3^2}$ describes its lumpiness. The last attribute, $class$, is set to 0 for all unclassified candidates. In classified data $class = 1$ indicates a crater and $class = 2$ indicates a non-crater feature.

Because a crater’s morphology depends on its size we have acquired three different training sets, one for crater candidates identified in C_{λ_1} , second for crater candidates identified in C_{λ_2} , and the third for crater candidates identified in $C_{\lambda \geq \lambda_3}$. The training sets are constructed iteratively. First a relatively small number of crater candidates is hand-labeled by a human expert and a classifier is built based on this initial training set. This classifier is then applied to all crater candidates in a given site and the results are visually reviewed and corrected if necessary. The corrected results constitute a new, much larger training set. This procedure is repeated for a number of sites. At present our three training sets contain 5970, 1010, and 431 examples, respectively. These training sets exemplify types of craters found in the eight test sites, and can be used for classification of crater candidates on in all similar surfaces.

We use decision trees to encapsulate data patterns present in our training sets. Decision trees are calculated using the C4.5 learning algorithm (Quinlan, 1993) as implemented in the software package WEKA (Witten and Frank, 2000). Fig. 2 (right) shows a

decision tree constructed by the C4.5 algorithm on the basis of 431 examples in the $C_{\lambda \geq \lambda_3}$ training set. The tree has 15 nodes and 8 leaves (terminal nodes). Feeding this tree with an unlabeled crater candidate detected in $C_{\lambda \geq \lambda_3}$ layers determines whether the candidate is a crater (terminal nodes denoted by 1) or non-crater feature (terminal nodes denoted by 2) with expected accuracy of 89%. Accuracy is measured using 10-fold cross-validation method (Kohavi, 1995). Fig. 2 (left) shows a decision tree constructed on the basis of 1010 examples in the C_{λ_2} training set. The tree has 25 nodes and 13 leaves; its expected accuracy is 90.1%. Finally, a decision tree constructed on the basis of 5970 examples in the C_{λ_1} training set (not shown here) has 59 nodes and 30 leaves, its expected accuracy is 96.2%. Applying the machine-learning algorithm to the Tisia Valles site (see Fig. 1) eliminates 10 objects from the list of crater candidates resulting in identification of 31 craters.

2.3. Cross-reference with the Barlow catalog

Cross-referencing craters identified by the AutoCrat with craters in the Barlow catalog is desirable not only for evaluation purposes but also for greater utility of the generated catalog. The locations of craters in the Barlow catalog are based on the MDIM 1.0 standard. However, the coordinates based on MDIM 1 differs from the coordinates based on the present, MDIM 2.1 standard due to improvements in geodetic control and changing definitions of cartographic parameters. Thus, using crater coordinates as given in the Barlow catalog, misplaces the crater on the modern map. Worse, the shift is not systematic making machine correction of coordinates in the Barlow catalog difficult. In order to cross-reference craters identified by the AutoCrat with craters in the Barlow catalog we have designed a semi-automatic procedure to correct coordinates of craters in the Barlow catalog. First a number of pairs of “control craters” are manually chosen for a given site. A pair of control craters consists of an entry from the Barlow catalog and an entry from our catalog that are judged to correspond to the same

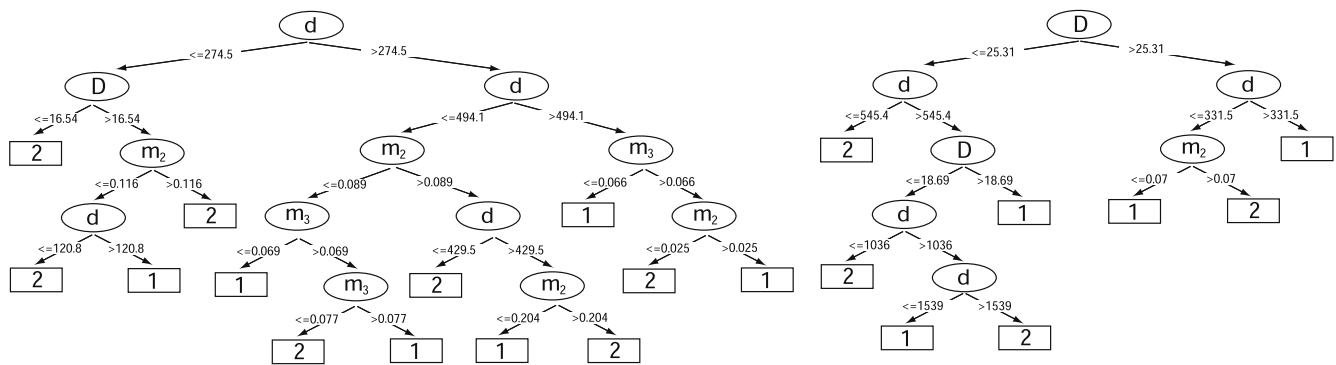


Fig. 2. Decision trees for selection of craters in the list of crater candidates detected in C_{i2} (left) and $C_{i>2}$ (right). The nodes of the trees are indicated by ovals; symbols inside ovals give split attributes (D —diameter, d —depth, m_2 and m_3 —shape descriptors). The terminal nodes (leaves) are shown as rectangles; leaves denoted 1 indicate craters, leaves denoted 2 indicate non-crater features. Depths are given in meters, diameters are given in kilometers.

actual crater. The coordinates of control craters are used to construct an interpolating function based on triangular interpolation. This function is used to rectify positions of all other entries in the Barlow catalog that belong to the site. Using corrected coordinates of entries in the Barlow catalog we match the entries in the two catalogs by means of the nearest neighbor algorithm. For each entry in the Barlow catalog we find a nearest neighbor from among entries in our catalog. If the nearest neighbor fulfills criteria for proximity and size similarity, the two entries are considered to correspond to the same crater.

3. Results

We have applied the AutoCrat system to eight test sites; the summary of the results are listed in Table 1. The sites' names and their locations are given in the first and the second column of the table, respectively. The first four sites are located in the Terra Cimmeria, progressively southward from the equator. All four Terra Cimmeria sites are dominated by heavily cratered Noachian terrain. The craters identified by our system in these four sites are depicted in Fig. 3. Note that for a crater to be identified by the AutoCrat system, it has to be located entirely within the boundaries of a site. The fifth and sixth sites in Table 1 feature less densely cratered Hesperian terrain; Fig. 4 shows craters identified by the AutoCrat in these two sites. Finally, the last two sites in Table 1 feature young, Amazonian, sparsely cratered terrain; the craters identified in these sites are shown in Fig. 5. The third column in Table 1 shows an approximate area of the sites, and the remaining columns show crater counts. The number of craters identified by the AutoCrat system is given in the fourth column, and the number of craters present in the Barlow catalog is given in the fifth column. The sixth column gives the number of craters identified by the AutoCrat and matched to craters in the Barlow catalog. The seventh column gives the number of craters identified by the AutoCrat but

absent from the Barlow catalog. Finally, the eighth column gives the number of craters that are present in the Barlow catalog, but were not identified by our system.

Overall, the AutoCrat system has identified 3666 craters in all eight sites in comparison to 2144 craters listed in the Barlow catalog, an increase of 71%. The system has identified 1544 (72%) craters listed in the Barlow catalog. The remaining 600, mostly heavily degraded craters present in the Barlow catalog have not been identified by our system. However, our system has identified 2122 “new” craters that are not listed in the Barlow catalog; these are mostly craters that are smaller than the 5-km-diameter lower limit of the Barlow catalog. The Barlow catalog contains craters as small as $D = 1.7$ km, and $\sim 8\%$ of all of its craters have $D < 5$ km, however this catalog is not intended to be complete for craters having diameter < 5 km. It is not possible to set beforehand a lower limit on the size of craters identified by the AutoCrat system. Setting $\lambda_1 = 5$ pixels (see Section 2.1) results in identification of craters with diameters as small as $D = 2.4$ km, and 40% of all craters identified by the AutoCrat have $D < 5$ km. Thus, the catalog created by the AutoCrat is “complete” down to a crater size smaller than $D = 5$ km, although the precise size limit of its completeness is difficult to assess.

Fig. 6 provides a more detailed comparison between our results and the Barlow catalog. Terrains of different ages (Noachian, Hesperian, and Amazonian) are compared separately, and we have divided all craters into five size-bins for a bin-by-bin comparison. On the Noachian surfaces, where degraded craters abound, the system identifies 70% of craters listed in the Barlow catalog, however, on the Hesperian and Amazonian surfaces, where fewer degraded craters are found, the system finds 85% of craters listed in the Barlow catalog. The AutoCrat identifies a lot of “new” craters, mostly in the $D < 5$ km bin-size (68% of new finds) and the 5–10 km size-bin (27% of new finds). On the Noachian surfaces the new finds constitute 92% of all the craters in the $D < 5$ km bin-size and 33% of all

Table 1
Comparison of crater counts.

Site name	Location: left (E), right (E), top (N), bottom (N)	Area 10^6 km^2	Craters AutoCrat	Craters Barlow	Craters matched	Craters AutoCrat only	Craters Barlow only
Terra Cimmeria 1	114.0, 141.4, -7.58 , -18.42	1.0	734	466	336	398	130
Terra Cimmeria 2	117.4, 145.4, -17.0 , -28.4	0.98	748	520	387	361	133
Terra Cimmeria 3	117.4, 145.4, -26.6 , -38.6	0.92	662	457	313	349	144
Terra Cimmeria 4	117.4, 145.4, -36.5 , -47.5	0.73	300	348	209	91	139
Hesperia Planum	107.1, 118.5, -17.0 , -29.6	0.44	305	119	102	203	17
Sinai Planum	261.5, 278.6, -10.3 , -29.7	1.0	468	101	94	374	7
Amazonis Planitia	195.0, 210.0, 30.0, 15.0	0.79	153	66	47	106	19
Olympica Fossae	240.0, 255.0, 30.0, 15.0	0.79	296	67	56	240	11
Total		6.65	3666	2144	1544	2122	600

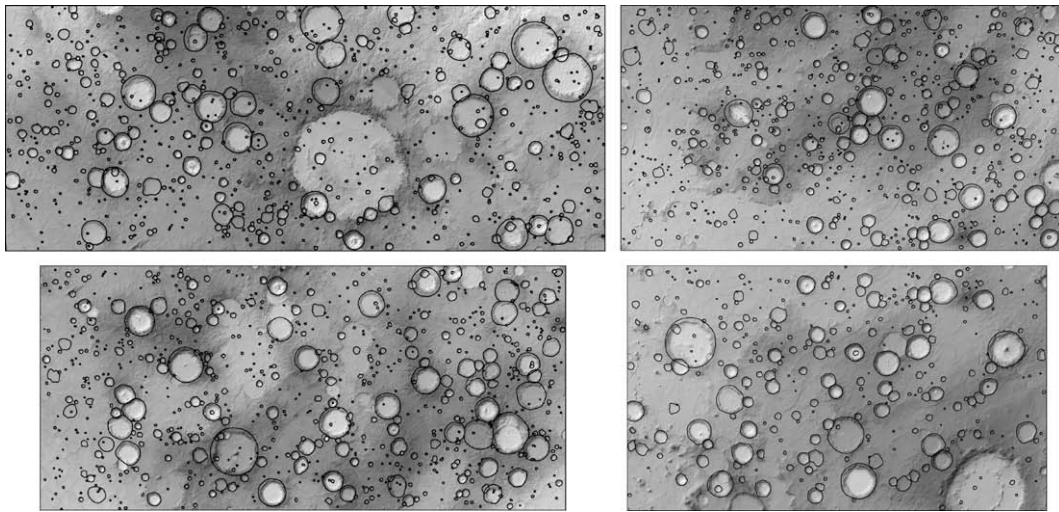


Fig. 3. Craters identified by the AutoCrat system in the Terra Cimmeria 1 site (top left), the Terra Cimmeria 2 site (bottom left), the Terra Cimmeria 3 site (top right), and the Terra Cimmeria 4 site (bottom right). The background shows the topography; high-to-low areas are depicted by dark-to-light grays.

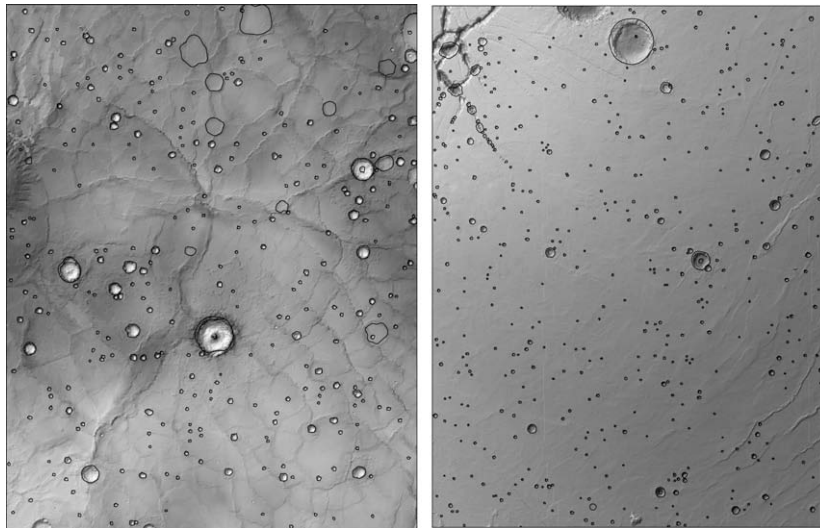


Fig. 4. Craters identified by the AutoCrat system in the Hesperia Planum site (left) and the Sinai Planum site (right). The background shows the topography; high-to-low areas are depicted by dark-to-light grays.

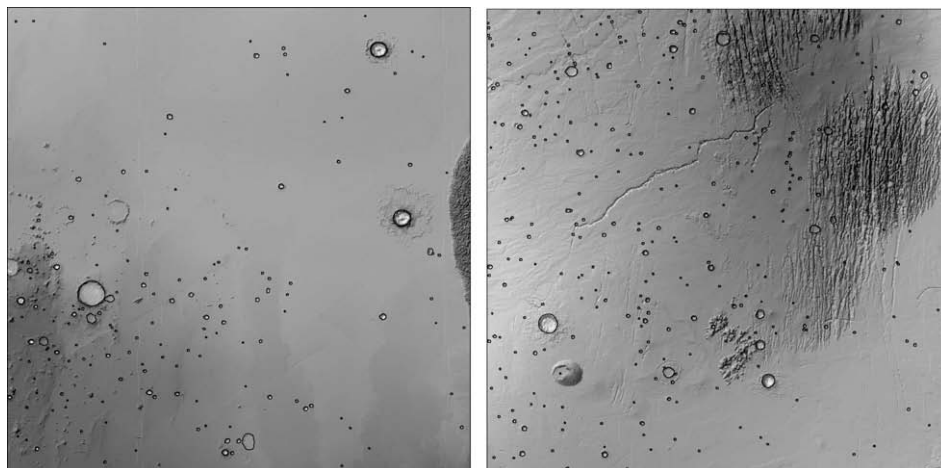


Fig. 5. Craters identified by the AutoCrat system in the Amazonis Planitia site (left) and the Olympica Fossae site (right). The background shows the topography; high-to-low areas are depicted by dark-to-light grays.

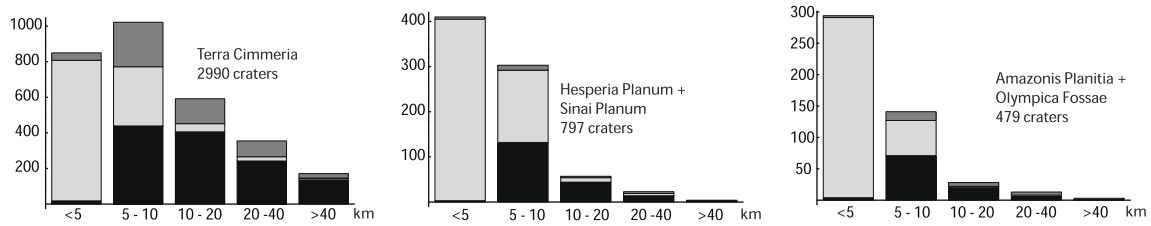


Fig. 6. Size-bin comparison of craters identified by the AutoCrat and listed in the Barlow catalog. Black indicates matched craters, light gray indicates craters not listed in the Barlow catalog, dark gray indicates craters not detected by the Autocrat.

the craters in the 5–10 km size-bin. On the Hesperian and Amazonian surfaces the new finds constitute 98% of all the craters in the $D < 5$ km bin-size and 52% of all the craters in the 5–10 km size-bin.

These results shows that the AutoCrat system identifies craters in a robust and predictable fashion. Using the $1/128^\circ$ topographic data it performs an exhaustive survey of (not heavily degraded) craters with diameter of about 3 km and larger. It fails to identify heavily degraded craters of all sizes and some less degraded, but very large craters. This is because such craters do not manifest themselves as detectable topographic depressions. Indeed, the overwhelming majority of false negatives are due to the failure of the system to detect a depression, and not due to the failure of the decision function. The system yields few false positives due to the superior performance of the machine-learning-based decision function.

In addition to identifying craters, the AutoCrat systems also calculates their diameters and depths. A crater diameter is calculated from the area of a depression. Fig. 7 (left) shows a comparison of the values of D_A , as calculated by our system, with the values of D_B , as given in the Barlow catalog, for 1544 craters for which both values are available. The best linear fit to the (D_A, D_B) data points is given by $D_B = 0.87D_A + 0.12$ that departs from an ideal statistical agreement given by a diagonal line $D_B = D_A$ and indicates that our system systematically overestimates the value of D by about 15%. The cause of this overestimation can be traced to the region expansion procedure (see Section 2.1) that favors overexpansion. Because this effect is systematic, calculated diameters can be rectified using transformation $D_A \rightarrow 0.87D_A + 0.12$. The average difference between the rectified values of D_A and the values of D_B is only 1.3%.

Crater depth is calculated as the difference between the highest and the lowest elevation in a depression. When calculating crater depths it is important to remember that the $1/128^\circ$ MEGDR, used in our calculations, is an interpolated grid. Although the along-the-track resolution of the MOLA data is ~ 330 m, the across-the-

track spacing is ~ 1000 m at the equator (Neumann et al., 2001). Some of the grid's pixels, having dimensions of 463×463 m on the equator, contain no direct elevation measurements, but instead are assigned an elevation value on the basis of interpolation from the nearby measurements. Therefore, in some locations, elevation values in several pixels constituting a small crater may be interpolated from measurement located outside this crater leading to a skewed measure of its' depth. Consequently, our estimates of depth for small craters should not be used individually, but only in the statistical context.

Fig. 7 (right) shows a comparison of the values of d_A , as calculated by our system, with the values of d_B , as calculated manually using the IMPACT software package, for 144 craters in the Hesperia Planum and Sinai Planum sites (J. Boyce, private communication). The IMPACT software (Mouginis-Mark et al., 2004) was developed to facilitate manual collection of geomorphic data for martian impact craters from the $1/128^\circ$ MEGDR. The best linear fit to the (d_A, d_B) data points is given by $d_B = 0.8d_A + 0.02$ that departs from an ideal statistical agreement given by a diagonal line $d_B = d_A$ and indicates that our system systematically “overestimates” the value of d by about 30%. Most of this difference can be attributed to different ways of measuring the depth; in IMPACT d_B is measured as the difference between an average elevation on the rim and the elevation of the crater floor, which, by definition, is smaller than d_A , calculated as the difference between the highest elevation on the rim and the lowest elevation on the crater floor. Because the difference between d_A and d_B is systematic, depths calculated by our system can be “rectified” by using transformation $d_A \rightarrow 0.8d_A + 0.02$. The average difference between the rectified values of d_A and the values of d_B is 11%.

4. Depth to diameter relationships

Impact craters are natural probes of martian surface properties and erosional processes (see Section 1). The crater depth to diameter ratio d/D is a simple yet particularly useful parameter to study

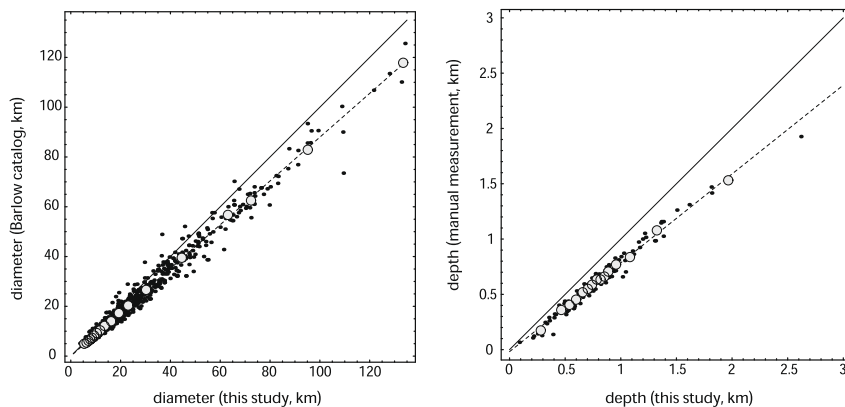


Fig. 7. (Left) A value of crater's diameter, D , as calculated automatically by the AutoCrat system versus a value of D as given in the Barlow catalog for all 1544 matched craters. (Right) A value of crater's depth, d , as calculated automatically by the AutoCrat system versus a value of d as given in the Boyce dataset of 144 craters. A dashed line shows the best linear fit and the solid line represents a diagonal. Individual craters are indicated by black dots; larger gray circles indicate a general trend.

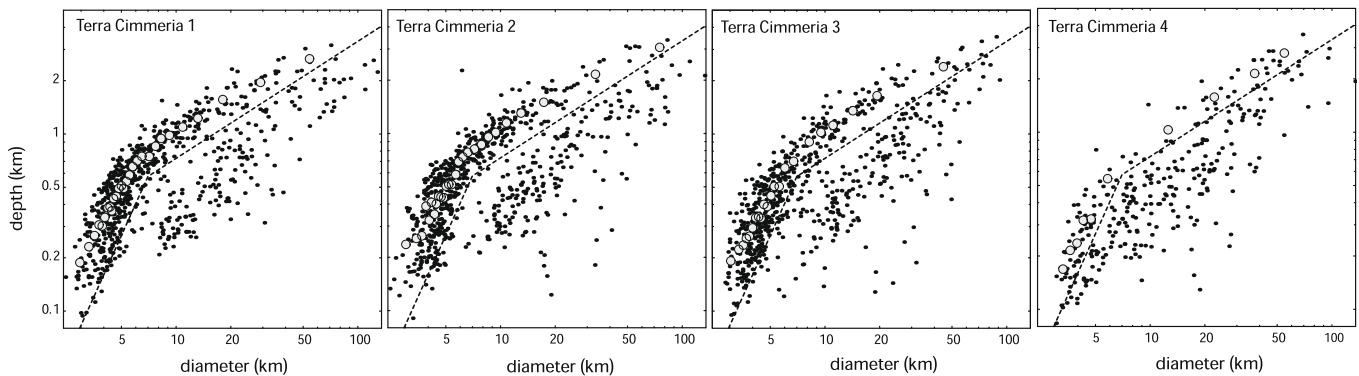


Fig. 8. Diameter–depth diagrams for the four Terra Cimmeria sites. The dashed lines represent curves separating deep craters from shallow craters. Gray circles indicate a trend calculated for deep craters by binning the data.

the geologic history of Mars. The importance of knowing the values of d/D lead to the establishment of a database of ~6000 fresh craters (located mostly in the northern hemisphere) for which depths were manually measured (Garvin et al., 2003; Boyce and Garbeil, 2007) from the MEGDR (using IMPACT), or from individual MOLA tracks. Using all craters in this database Garvin et al. (2003) have calculated the best-fit relationship between d and D to be $d = 0.21D^{0.81}$ for simple craters ($D < 6$ km), and $d = 0.36D^{0.49}$ for complex craters ($D \geq 6$ km). Using values of (D, d) calculated by the AutoCrat for 3666 craters found in our eight test sites we have calculated $d = 0.025D^{1.6}$ for simple craters ($D < 7$ km), and $d = 0.22D^{0.47}$ for complex craters ($D \geq 7$ km). Thus, our data and the manually collected data yield very similar d – D relationships for complex craters, but different relationships for simple craters. Three factors may explain these differences. First, the manual database is restricted to fresh craters whereas automatic survey includes craters at all stages of preservation. Second, our data extends to smaller craters, which may be shallower than indicated by a relationship established for larger (but still simple) craters, as the smaller craters are more prone to erosion. Third, in the MEGDR small craters may appear systematically shallower due to the coarseness of the grid.

Fig. 8 shows the d – D diagrams for the four Terra Cimmeria sites. The first observation is that the craters in the first three Terra Cimmeria sites split into two, easily identifiable populations of deep craters and shallow craters. The dashed lines on Fig. 8 represent a curve separating the population of deep craters (above the curve) from the population of shallow craters (below the curve). The percentage of craters in each population and exponents characterizing the d – D relationships for deep craters are given in Table 2. The deep craters can be interpreted as fresh and the shallow craters can be interpreted as degraded, however it is important to stress that the present automatic system has no means to assess crater morphology beyond calculating values of D and d . The second observation is that in the Terra Cimmeria the percentage of deep

craters decreases southwards (see Table 2). In fact, the character of d – D diagram for the Terra Cimmeria 4 site, located between 36.5°S and 47.5°S is qualitatively different from characters of the (D, d) diagrams for the other three sites located to the north. In the Terra Cimmeria 4 site no two distinguished populations of craters are observed, and the number of deep craters (so-defined by being located above the dashed line on Fig. 8) is much reduced.

In Fig. 9, we plot d/D as a function of latitude for 2444 craters in the four Terra Cimmeria sites. The craters defined as deep are plotted as black dots and the craters defined as shallow are plotted as gray dots. The larger circles represented trends calculated from binning the data. This figure shows that deep craters of all sizes in the Terra Cimmeria start to be depleted southward of ~26°S, and severely depleted southward of ~38°S. Mouginis-Mark and Hayashi (1993) studied latitudinal variations of d/D for 109 craters located in Hesperia Planum between 20°S and 40°S. They also found a general shallowing of craters with increasing latitude, although (possibly due to a small number of craters in their sample) they did not find an abrupt change like the one present in our Terra Cimmeria data. Mouginis-Mark and Hayashi attributed the observed shallowing of craters to a poleward increase of sub-surface ice. Boyce et al. (2004) calculated d/D values for 460 craters located in Noachian age regions of Thyles Rupes and Prometheus between 70°S and 80°S. Although they did not study the latitudinal variations of d/D within these sites, they found the craters in these regions to be systematically shallower than craters at equatorial regions having similar geologic history (Sinai Planum). They also attributed these findings to poleward increase of sub-surface ice. If the southward shallowing of craters in Terra Cimmeria is likewise attributed to the presence of sub-surface ice, an abrupt change in spatial distribution of ice at 38°S is indicated by our results. Alternatively, the observed paucity of deep craters south of ~40°S can be explained in terms of a surficial mantling deposit (Soderblom et al., 1973).

Fig. 10 shows the d – D diagrams for the four remaining (Hesperian and Amazonian age) sites in our study. The dashed lines in Fig. 10 represent the deep/shallow crater separation curve as established on the basis of the Terra Cimmeria sites. The percentage of craters in each population and exponents characterizing the d – D relationships for deep craters are given in Table 2. It is clear that the younger surfaces contain mostly deep craters supporting our interpretation of shallow craters as mostly degraded (older) craters. However, the exponents characterizing the d – D on these surfaces are not significantly different from exponents characterizing d – D on older surfaces. This is in agreement with the findings of Boyce et al. (2004) who compared craters in Sinai Planum to craters in Noachian age sites located at southern high latitudes (see above).

Table 2
Deep and shallow craters.

Site name	Deep name (%)	Shallow name (%)	Simple craters exponent	Complex craters exponent
Terra Cimmeria 1	74	26	1.79	0.60
Terra Cimmeria 2	70	30	1.62	0.56
Terra Cimmeria 3	66	34	1.72	0.57
Terra Cimmeria 4	32	68	2.00	0.67
Hesperia Planum	86	14	1.75	0.63
Sinai Planum	85	15	1.84	0.73
Amazonis Planitia	80	20	2.01	0.60
Olympica Fossae	77	23	1.81	0.52

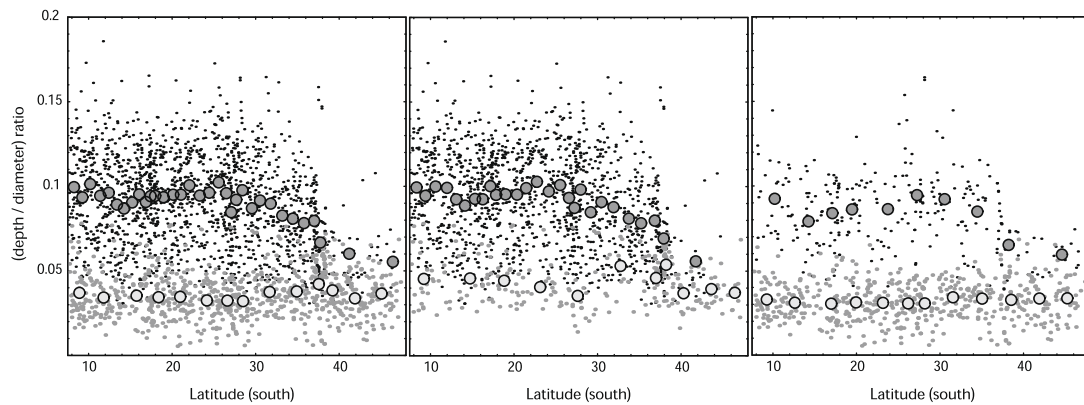


Fig. 9. Dependence of d/D on latitude for 2444 craters in all Terra Cimmeria sites (left panel). Black dots indicate deep craters, gray dots indicate shallow craters, circles indicate trends calculated by binning the data. Middle panel shows only craters with $D < 10$ km and the right panel shows only craters with $D \geq 10$ km.

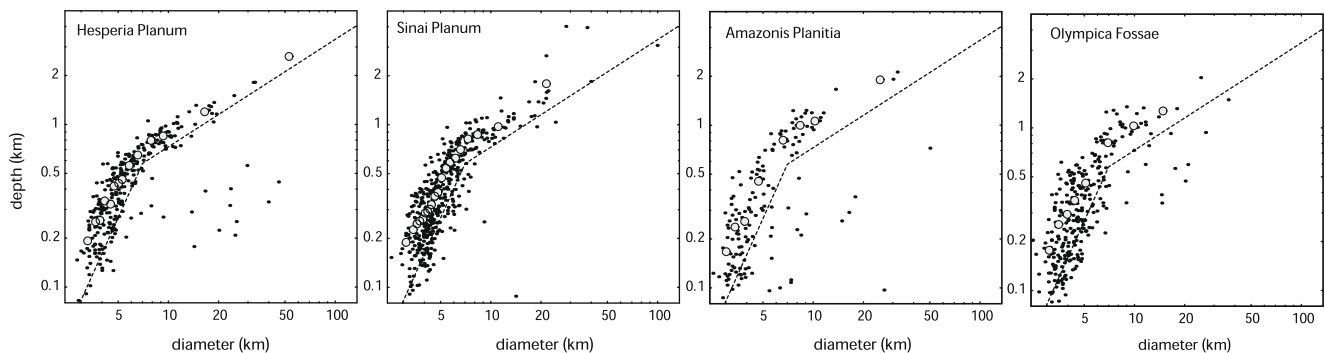


Fig. 10. Diameter–depth diagrams for the Hesperian and Amazonian sites in our study. The dashed lines represent curves separating deep craters from shallow craters. Gray circles indicate a trend calculated for deep craters by binning the data.

5. Discussion

The AutoCrat system is a robust and practical CDA designed especially for global surveys of impact craters on Mars but applicable to any surface represented by a DEM. A computer code implementing the depression-finding module of the AutoCrat is available at cratermatic.sourceforge.net. The crater-selecting module is implemented using WEKA software that is available at www.cs.waikato.ac.nz/ml/weka/. Whereas previously developed CDAs were image-based, the AutoCrat catalogs craters from DEM data. The AutoCrat works on different principles than another DEM-based CDA which we have developed earlier (Bue and Stepinski, 2007); its methods bear no resemblance to methods employed by image-based CDAs. The most important features of the AutoCrat system are: robustness, minimization of false positive detections, and seamless integration of craters detection with their topographic characterization. As we have shown in Section 3, the system is robust inasmuch as it works equally well on all types of martian surfaces, without any changes to its parameters. This feature sets it apart from image-based CDAs, as well as our earlier DEM-based algorithm; all these CDAs need parameter readjustment when applied to different surfaces making them impractical for global surveys. AutoCrat achieves detection accuracy on par with the best image-based CDAs without readjustment of parameters. Because our system employs a machine-learning-based decision function based on an extensive training set, there are virtually no false positive detections in catalogs produced by the AutoCrat. However, the system produces some false negatives—craters that do not appear as round and symmetric depressions in a DEM. These are mostly heavily degraded or highly irregular craters. Fi-

nally, the system measures diameters and depths of craters on-the-fly, as they are identified.

We have demonstrated the utility of our system by machine cataloging craters in eight large sites. One of these sites—Terra Cimmeria 1—is the same site used in Bue and Stepinski (2007) to assess the performance on our initial version of a DEM-based CDA. The initial CDA has identified 603 “craters” in this site, 135 of which was judged as false positives. The AutoCrat has identified 734 craters in this site with no false positives. However, the biggest practical advantage of the AutoCrat is its robustness; the system works well for all sites on Mars, even if its accuracy depends on the character of the surface. The initial CDA was not robust, its application to sites other than the Terra Cimmeria 1 produced very poor results. The robustness of the AutoCrat system is due to the use of decision function generated by a machine-learning technique.

To demonstrate the utility of the AutoCrat-generated catalog of craters we have employed it to construct d – D diagrams and to derive the relationships between d and D . Our findings confirm some of the earlier results (Mouginis-Mark and Hayashi, 1993; Craddock et al., 1997; Boyce et al., 2004, 2006) regarding absence of deep craters at mid and high southern latitudes. The ability of the AutoCrat to provide an estimate of d for all the craters in the Terra Cimmeria region resulted in a clear and unambiguous demonstration of an abrupt change in crater depths at the latitude of $\sim 38^\circ\text{S}$.

Despite its robustness, the AutoCrat system, in its present (“Version 1.0”) form is not a replacement for manual cataloging because of its limitations in detectability as well as characterization of craters. The system will not detect highly degraded craters or even fresh but elliptical craters. It is restricted to calculating crater

size, its depth, and a measure of its shape, but it cannot provide information about crater morphology or freshness. Thus, we envision the present version of AutoCrat to serve as a tool that supplements rather than replaces manual surveys. For example, it can provide a “first draft” of the catalog which can be subsequently edited and enhanced by an analyst. The future research on AutoCrat will address some of its limitations. One line of work will focus on developing capabilities for calculating more topographic attributes characterizing each crater candidate which will allow for more precise decision function resulting in improved detectability of craters. Our recent work on segmentation-based classification of landforms (Stepinski et al., 2006) can be used to automatically recognize various parts of a crater, a crucial first step for automatic calculation of these attributes. Another line of work will focus on feasibility of automatic detection of crater morphology using methods inspired by the face recognition problem.

One shortcoming of using the AutoCrat to catalog craters on Mars is a coarse resolution of presently available martian DEM, which limits the size of craters identifiable by the system to $D \geq 2.5$ km. A reliable estimate of crater depth is probably limited to craters with $D \geq 5$ km. The advantage of automatic system becomes fully apparent in surveying a very large number of smaller crater—a task beyond practical means of human analysts. The AutoCrat system is scale-independent and is expected to work without modification using higher resolution DEMs. Such DEMs are now becoming available for extensive portions of martian surface using stereo images taken by the High Resolution Stereo Camera (HRSC) (Albertz et al., 2005) onboard the Mars Express spacecraft. Using a DEM with resolution of 100 m, the AutoCrat is expected to catalog craters with $D \geq 500$ m and to obtain a reliable values of depths for craters with $D \geq 1$ km. Even smaller craters could be cataloged by AutoCrat using DEMs constructed from stereo data obtained by the Mars Reconnaissance Orbiter's HiRISE camera. Future research will assess applicability of the AutoCrat for cataloging craters using HRSC-derived and HiRISE-derived DEMs. The system can also be utilized for cataloging craters on the Moon and on the planet Mercury once high resolution DEMs of their surfaces become available.

Acknowledgments

This work was supported by National Science Foundation under Grant IIS-0430208 and by NASA under Grant NNG06GE57G. The presented research was conducted at the Lunar and Planetary Institute, which is operated by the USRA under Contract CAN-NCC5-679 with NASA, This is LPI Contribution No. 1345.

References

- Albertz, J. the HRSC, Col Team, 2005. HRSC, on Mars Express—Photogrammetric and cartographic research. *Photogrammetric Eng. Remote Sens.* 71 (10), 1153–1166.
- Barata, T., Ivo Alves, E., Saraiva, J., Pina, P., 2004. Automatic recognition of impact craters on the surface of Mars. In: *Proceedings of the Image Analysis and Recognition: International Conference ICIAR 2004*, Porto, Portugal, pp. 489–496.
- Barlow, N.G., 1988. Crater size-distributions and a revised martian relative chronology. *Icarus* 75 (2), 285–305.
- Barlow, N.G., 2005. A review of martian impact crater ejecta structures and their implications for target properties. In: *Large Meteorite Impacts III*, Geological Society of America Special Paper, vol. 384, pp. 433–442.
- Barlow, N.G., 2006. Status Report on the “Catalog of Large Martian Impact Craters”, Version 2.0. *Lunar and Planetary Science XXXVII*, # 1337, Lunar and Planetary Institute, Houston.
- Barlow, N.G., Perez, C.B., 2003. Martian impact crater ejecta morphologies as indicators of the distribution of subsurface volatiles. *J. Geophys. Res.* 108 (E8), 5085, doi:10.1029/2002JE002036.
- Boyce, J.M., Garbeil, H., 2007. Depth to diameter relationships of prestine martian complex impact craters: Implication to crater mechanics, surface properties and surface process studies. *Lunar and Planetary Science XXXVIII*, # 1931, Lunar and Planetary Institute, Houston.
- Boyce, J.M., Mouginiis-Mark, P., Garbeil, H., 2004. Depth to diameter relationships of craters in the high latitudes (70°–80°) of Mars: Implications for geologic history of those areas. *Lunar and Planetary Science XXXV*, # 1129, Lunar and Planetary Institute, Houston.
- Boyce, J.M., Mouginiis-Mark, P., Garbeil, H., 2005. Ancient oceans in the northern lowlands of Mars: Evidence from impact crater depth/diameter relationships. *J. Geophys. Res.* 110, E03008.
- Boyce, J.M., Mouginiis-Mark, P., Garbeil, H., 2006. History of major crater degradational events on Mars: Preliminary results from crater depth and diameter measurements. *Lunar and Planetary Science XXXVII*, # 2354, Lunar and Planetary Institute, Houston.
- Bue, B.D., Stepinski, T.F., 2007. Machine detection of martian impact craters from digital topography data. *IEEE Trans. Geosci. Remote Sens.* 45 (1), 265–274.
- Burl, M.C., Stough, T., Colwell, W., Bierhaus, E.B., Merline, W.J., Chapman, C., 2001. Automated detection of craters and other geological features. In: *Proceedings of the International Symposium on Artificial Intelligence, Robotics and Automation for Space*, Montreal, Canada.
- Cheng, Y., Johnson, A.E., Matthies, L.H., Olsen, C.F., 2003. Optical landmark detection for spacecraft navigation. In: *Proceedings of the 13th AAS/AIAA Space Flight Mechanics Meeting*, Ponce, Puerto Rico, AAS 03-224, pp. 1785–1803.
- Cintala, M.J., Mouginiis-Mark, P.J., 1980. Martian fresh crater depth: More evidence for subsurface volatiles. *Geophys. Res. Lett.* 7, 329–332.
- Cintala, M.J., Head, J.W., Mutch, T.A., 1976. Martian crater depth/diameter relationship: Comparison with the Moon and Mercury. *Proc. Lunar Sci. Conf.* 7, 3375–3587.
- Costard, F.M., 1989. The spatial distribution of volatiles in the martian hydrosphere. *Earth Moon Planets* 45, 265–290.
- Craddock, R.A., Maxwell, T.A., Howard, A.D., 1997. Crater morphometry and modification in the Sinus Sabaeus and Margaritifer Sinus regions on Mars. *J. Geophys. Res.* 102 (E6), 13321–13340.
- Crater Analysis Technique Working Group, 1979. Standard techniques for presentation and analysis of crater size-frequency data. *Icarus* 37, 467–474.
- Forsberg-Taylor, N.K., Howard, A.D., Craddock, R.A., 2004. Crater degradation in the martian highlands: Morphometric analysis of the Sinus Sabaeus region and simulation modeling suggest fluvial process. *J. Geophys. Res.* 109, E05002, doi:10.1029/2004JE002242.
- Garvin, J.B., Frawley, J.J., 1998. Geometric properties of martian impact craters: Preliminary results from the Mars orbiter laser altimeter. *Geophys. Res. Lett.* 25, 4405–4408.
- Garvin, J.B., Sakimoto, S.E.H., Frawley, J.J., Schnetzler, C., 2000. North polar region craterforms on Mars: Geometric characteristics from the Mars orbiter laser altimeter. *Icarus* 144, 329–352.
- Garvin, J.B., Sakimoto, S.E.H., Frawley, J.J., 2003. Craters on Mars: Global geometric properties from gridded MOLA topography. In: *6th International Conference on Mars*, # 3277, Lunar and Planetary Institute, Houston.
- Hartmann, W.K., Neukum, G., 2001. Cratering chronology and the evolution of Mars. *Space Sci. Rev.* 96, 165–194.
- Honda, R., Iijima, Y., Konishi, O., 2002. Mining of Topographic Feature from Heterogeneous Imagery and Its Application to Lunar Craters, *Progress in Discovery Science: Final Report of the Japanese Discovery Science Project*. Springer, p. 395.
- Kieffer, S.W., Simonds, C.H., 1980. The role of volatiles and lithology in the impact cratering process. *Rev. Geophys. Space Phys.* 18, 143–181.
- Kim, J.R., Muller, J.-P., van Gasselt, S., Morley, J.G., Neukum, G. the HRSC Col Team, 2005. Automated crater detection, a new tool for mars cartography and chronology. *Photogrammetric Eng. Remote Sens.* 71 (10), 1205–1217.
- Kohavi, R., 1995. A study of cross-validation and bootstrap for accuracy estimation and model selection. In: *Proceedings of XIV International Joint Conference on Artificial Intelligence*, vol. 2, no. 12, pp. 1137–1143.
- Kuzmin, R.O., Bobina, N.N., Zabalueva, E.V., Shashkina, V.P., 1988. Structural inhomogeneities of the martian cryosphere. *Solar System Res.* 22, 121–133.
- Leroy, B., Medioni, G., Johnson, A.E., Matthies, L.H., 2001. Crater detection for autonomous landing on asteroids. *Image Vis. Comput.* 19, 787–792.
- Mouginiis-Mark, P.J., Hayashi, J.N., 1993. Shallow and deep fresh impact craters in Hesperia Planum, Mars. *Earth Moon Planets* 61 (1), 1–20.
- Mouginiis-Mark, P.J., Garbeil, H., Boyce, J.M., Ui, C.S.E., Baloga, S.M., 2004. Geometry of martian impact craters: First results from an interactive software package. *J. Geophys. Res.* 109, E08006.
- Neumann, G.A., Rowlands, D.D., Lemoine, F.G., Smith, D.E., Zuber, M.T., 2001. Crossover analysis of MOLA altimetric data. *J. Geophys. Res.* 106, 23735–23768.
- O'Callaghan, J.F., Mark, D.M., 1984. The extraction of drainage networks from digital elevation data. *Comput. Vis. Graph. Image Process.* 28, 328–344.
- Pike, R.J., Davis, P.A., 1984. Toward a topographic model of martian craters from photoclinometry. *Lunar and Planetary Science XV* 645–646, Lunar and Planetary Institute, Houston.
- Plesko, C., Brumby, S., Asphaug, E., Chamberlain, D., Engel, T., 2004. Automatic crater counts on mars. *Lunar and Planetary Science XXXV*, #1935, Lunar and Planetary Institute, Houston.
- Quinlan, J.R., 1993. C4.5: Programs for Machine Learning. Morgan Kaufmann, San Francisco.
- Reiss, D., van Gasselt, S., Hauber, E., Michael, G., Jaumann, R., Neukum, G., 2006. Ages of rampart craters in equatorial regions on Mars: Implications for the past and present distribution of ground ice. *Meteoritics Planet. Sci.* 41 (10), 1437–1452.
- Roddy, D.J., Isbell, N.R., Mardock, C.L., Hare, T.M., Wyatt, M.B., Soderblom, L.M., Boyce, J.M., 1998. Martian impact craters, ejecta blankets, and related morphologic features: Computer digital inventory in arc/info and Arcview format. *Lunar and Planetary Science XXIX*, #1874, Lunar and Planetary Institute, Houston.

- Rodionova, J.F., Dekchtyareva, K.I., Khramchikhin, A.A., Michael, G.G., Ajukov, S.V., Pugacheva, S.G., Shevchenko, V.V., 2000. Morphological Catalogue of the Craters of Mars. ESA-ESTEC.
- Salamuniccar, G., Loncaric, S., 2008. GT-57633 catalogue of martian impact craters developed for evaluation of crater detection algorithms. *Planet. Space Sci.* 56, 1992–2008.
- Smith, D., Neumann, G., Arvidson, R.E., Guinness, E.A., Slavney, S., 2003. Mars Global Surveyor Laser Altimeter Mission Experiment Gridded Data Record. NASA Planetary Data System, MGS-M-MOLA-5-MEGDR-L3-V1.0.
- Soderblom, L.A., Kreidler, T.J., Masursky, H., 1973. Latitudinal distribution of a debris mantle on the martian surface. *J. Geophys. Res.* 78 (20), 4117–4122.
- Soderblom, L.A., Condit, C.D., West, R.A., Herman, B.M., Kreidler, T.J., 1974. Martian planetwide crater distributions: Implications for geologic history and surface processes. *Icarus* 22, 239–263.
- Stepinski, T.F., Ghosh, S., Vilalta, R., 2006. Automatic recognition of landforms on Mars using terrain segmentation and classification. In: *Proceedings of the International Conference on Discovery Science*, LNAI 4265, pp. 255–266.
- Stewart, S.T., Valiant, G.J., 2006. Martian subsurface properties and crater formation process inferred from fresh impact geometries. *Meteoritics Planet. Sci.* 41 (10), 1509–1537.
- Tanaka, K.L., 1986. The stratigraphy of Mars. *J. Geophys. Res.* 91 (Suppl.), E139–E158.
- Vinogradova, T., Burl, M., Mjosness, E., 2002. Training of a crater detection algorithm for Mars crater imagery. In: *Aerospace Conference Proceedings*, 2002, vol. 7. IEEE, pp. 7-3201–7-3211.
- Wetzler, P.G., Enke, B., Merline, W.J., Chapman, C.R., Burl, M.C., 2005. Learning to detect small impact craters. In: *Seventh IEEE Workshops on Computer Vision (WACV/MOTION'05)*, vol. 1, pp. 178–184.
- Wise, D.U., Minkowski, G., 1980. Dating methodology of small, homogeneous crater populations applied to the Tempe-Utopia Trough region on Mars. *NASA Tech. Memo* 81776, 122–124.
- Witten, I.H., Frank, E., 2000. *DataMining: Practical Machine Learning Tools and Techniques with Java Implementations*. Academic Press, London, UK.